

Article

The Crystal Structure of 2-Amino-4-(2,3-Dichlorophenyl)-6-Methoxy-4*H*-Benzo[*h*]chromene-3-Carbonitrile: Antitumor and Tyrosine Kinase Receptor Inhibition Mechanism Studies

Ahmed M. El-Agrody ^{1,*}, Ahmed M. Fouda ², Hany M. Mohamed ^{1,3}, Mohammed Y. Alshahrani ⁴, Hazem A. Ghabbour ⁵, Abd El-Galil E. Amr ^{6,7,*}, Rawda M. Okasha ⁸, Ahmed M. Naglah ^{6,7}, Abdulrahman A. Almehezia ⁶ and Ahmed A. Elhenawy ^{1,9,*}

- ¹ Chemistry Department, Faculty of Science, Al-Azhar University, Nasr City, Cairo 11884, Egypt; hanysm83@yahoo.com
- ² Chemistry Department, Faculty of Science, King Khalid University, Abha 61413, Saudi Arabia; amfouda@hotmail.com
- ³ Chemistry Department, Faculty of Science, Jazan University, Jazan 45142, Saudi Arabia
- ⁴ Department of Clinical Laboratory Science, College of Applied Medical Science, King Khalid University, Abha 61413, Saudi Arabia; moyahya@kku.edu.sa
- ⁵ Department of Medicinal Chemistry, Faculty of Pharmacy, University of Mansoura, Mansoura 35516, Egypt; ghabbourh@yahoo.com
- ⁶ Pharmaceutical Chemistry Department, Drug Exploration and Development Chair (DEDC), College of Pharmacy, King Saud University, Riyadh 11451, Saudi Arabia; anaglah@ksu.edu.sa (A.M.N.); mehizia@ksu.edu.sa (A.A.A.)
- ⁷ Applied Organic Chemistry Department, National Research Centre, Giza 12622, Egypt
- ⁸ Chemistry Department, Faculty of Science, Taibah University, Medina 30002, Saudi Arabia; rawdao@yahoo.com
- ⁹ Chemistry Department, Faculty of Science and Art, AlBaha University, Al Bahah 65731, Saudi Arabia
- * Correspondence: elagrody_am@azhar.edu.eg (A.M.E.-A.); aamr@ksu.edu.sa (A.E.-G.E.A.); elhenawy_sci@hotmail.com (A.A.E.)



Citation: El-Agrody, A.M.; Fouda, A.M.; Mohamed, H.M.; Alshahrani, M.Y.; Ghabbour, H.A.; Amr, A.E.-G.E.; Okasha, R.M.; Naglah, A.M.; Almehezia, A.A.; Elhenawy, A.A. The Crystal Structure of 2-Amino-4-(2,3-Dichlorophenyl)-6-Methoxy-4*H*-Benzo[*h*]chromene-3-Carbonitrile: Antitumor and Tyrosine Kinase Receptor Inhibition Mechanism Studies. *Crystals* **2022**, *12*, 737. <https://doi.org/10.3390/cryst12050737>

Academic Editors: Mohammed Rafi Shaik, Syed Farooq Adil, Mujeeb Khan, Dinadayalane Tandabany and Waldemar Maniukiewicz

Received: 28 March 2022

Accepted: 10 May 2022

Published: 20 May 2022

Publisher's Note: MDPI stays neutral with regard to jurisdictional claims in published maps and institutional affiliations.



Copyright: © 2022 by the authors. Licensee MDPI, Basel, Switzerland. This article is an open access article distributed under the terms and conditions of the Creative Commons Attribution (CC BY) license (<https://creativecommons.org/licenses/by/4.0/>).

Abstract: The target compound, 2-amino-4-(2,3-dichlorophenyl)-6-methoxy-4*H*-benzo[*h*]chromene-3-carbonitrile (**4**), was synthesized via the reaction of 4-methoxynaphthalen-1-ol (**1**), 2,3-dichlorobenzaldehyde (**2**), and malononitrile (**3**) in an ethanolic piperidine solution under microwave irradiation. The synthesized β -enaminonitrile derivative (**4**) was characterized by spectral data and X-ray diffraction. The *in vitro* anti-proliferative profile was conducted against five cancer cell lines and was assessed for compound **4**, which revealed strong and selective cytotoxic potency. This derivative showed promising inhibition efficacy against the EGFR and VEGFR-2 kinases in comparison to Sorafenib as a reference inhibitor. Lastly, the docking analysis into the EGFR and VEGFR-2 active sites was performed to clarify our biological findings.

Keywords: benzochromenes; antitumor activity; EGFR; VEGFR-2; docking; X-ray

1. Introduction

Chromenes and benzochromenes are located in a wide range of natural products [1–5] and have diverse biological actions. These molecules have demonstrated remarkable anticancer activities through their resistance against specific enzymes such as steroid sulfatase, aromatase, and/or carbonic anhydrase [6–8]. 4*H*-Benzo[*h*]chromene derivatives exhibit anticancer activities. Case in point, the 4-aryl-substituted 4*H*-benzo[*h*]chromene and 6-chloro-substituted 4*H*-benzo[*h*]chromene derivatives operate as tumor vascular-disrupting-agents (VDA) and induce cell cycle arrest via the G2/M phases [9]. Additionally, the 4-pyridin-3-yl derivative of 4*H*-benzo[*h*]chromene is a potent inhibitor of cell proliferation and causes accumulation of smooth muscle cells at the G2/M phase as well as induces mitotic arrest in Chinese hamster ovary cells and HeLa cells, which has been

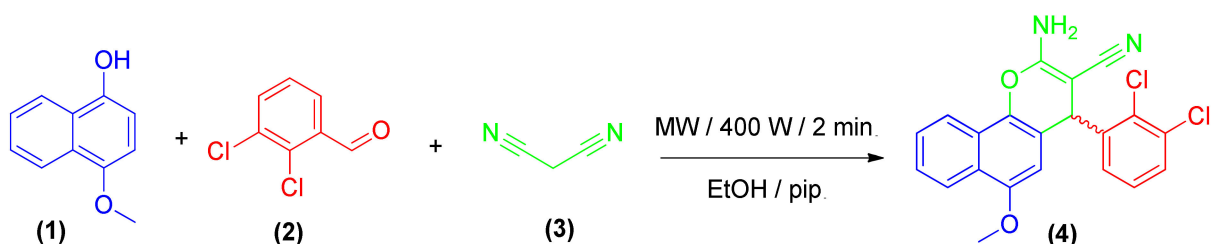
revealed in the molecule's cell cycle analysis [10]. Furthermore, the 4-aryl-substituted and ester derivatives of 4*H*-benzo[*h*]chromene exhibit good cytotoxic and apoptotic effects on a variety of human cancer cell lines [11,12]. Similarly, the 6-chloro, 6-methoxy, and ester derivatives of 4*H*-benzo[*h*]chromene [13–16] alongside the ester molecules of the 2,7-diamino-4*H*-benzo[*h*]chromene derivatives [12] demonstrated active cytotoxicity against MCF-7, HCT-116, and HepG-2 tumorous cell lines. Moreover, the 2-acetylamino and 2-aminomethyleneamino derivative of 6-methoxy-4*H*-benzo[*h*]chromene have been reported regarding their active cytotoxic behavior, cell cycle progression impact, induced apoptosis in human cancer cell lines, and inhibition of the topoisomerase enzyme [17]. In addition to the previous examples, chromene derivatives continue to be one of the most richly researched areas within contemporary literature. As precedingly established, these molecules have been incorporated in diverse functionalities, such as the enhancement of the antitumor agent's efficiency, inhibition of the *c*-Src kinase, DNA-binding and Bcl-2-protein inhibitor activities [18,19], induction of cell cycle arrest and apoptosis in human cancer cells via dual inhibition of topoisomerase I/II, caspase 3/7 activity, and DNA fragmentation [12,20–25].

Through the aforesaid instances and as a part of our ongoing interest in the generation of new pyran derivatives with promising biological activities [26–50], the following report reflects the central objective of synthesizing 2-amino-4-(2,3-dichlorophenyl)-6-methoxy-4*H*-benzo[*h*]chromene-3-carbonitrile (**4**). An *in vitro* anti-proliferative profile was executed against five cancerous cell lines and two normal (standard) cell lines for derivative **4**. Additionally, the inhibition efficiency of the EGFR and VEGFR-2 tyrosine kinase receptors was explored and evaluated against Sorafenib as a reference inhibitor. The molecular docking into the active sites of EGFR and VEGFR-2 was applied in order to introduce a reasonable clarification for the findings.

2. Results and Discussion

2.1. Chemistry

Scheme 1 illustrates the preparation route for molecule **4**. Synthesis was initiated by the reaction of 4-methoxynaphthalen-1-ol (**1**) with 2,3-dichlorobenzaldehyde (**2**) and malononitrile (**3**) in an ethanolic-piperidine media under microwave irradiation conditions to afford 2-amino-4-(2,3-dichlorophenyl)-6-methoxy-4*H*-benzo[*h*]chromene-3-carbonitrile (**4**). By repeating the reaction at different watt powers (200, 300, 400 W) and time intervals, the maximal power of microwave irradiation was maximized (1, 1.5, 2 min.). The best results were obtained by employing 400 W with a 2 min. reaction period, which gave the maximum yield for compound **4**. TLC was employed to monitor the reaction.



Scheme 1. Synthesis of 2-amino-4-(2,3)-dichlorophenyl)-6-methoxy-4*H*-benzo[*h*]chromene-3-carbonitrile (**4**).

The specific rotation for derivative **4** was determined to detect the stereochemistry, which showed zero rotation. This indicates that compound **4** is optically inactive and is obtained in the racemic mixture form (\pm); Scheme 1 [48–50].

2.2. Spectroscopic Data

The structure and purity of molecule **4** was investigated through spectroscopic data analyses. The IR-spectrum of **4** exhibited characteristic absorption-bands at ν 3336, 3211 cm^{-1}

for NH₂ and 2188 cm⁻¹ for the CN groups. Moreover, the ¹H NMR-spectra of **4** revealed singlet signals of the amino, methine, and methoxy moiety protons at δ 7.19 (D₂O exchangeable), 5.45, and 3.78 ppm, respectively. Meanwhile, the ¹³C NMR-spectra of **4** displayed the signals of the methine and methoxy carbons at δ 55.66 and 54.50 ppm. Furthermore, the MS, ¹³C NMR-DEPT/APT, and X-ray single crystal analyses of **4** delivered the absolute confirmation for their structures (see Supplementary Materials, Figures S1–S7).

2.3. Biological Activity

2.3.1. Cell Viability Assay

Compound **4** was evaluated in an initial screening for its anticancer properties against five human cancerous cell lines: mammary gland breast cancer (MCF-7), human colon cancer (HCT-116), human prostate adenocarcinoma metastatic (PC-3), lung carcinoma (A549), and liver cancer (HepG-2) in comparison with Vinblastine and Colchicine as reference drugs. Compound **4** was further evaluated against two normal cell lines: human fetal lung (HFL-1) and human diploid fibroblasts (WI-38). The 3-(4,5-dimethylthiazol-2-yl)-2,5-diphenyltetrazolium bromide (MTT) colorimetric assay [51] was performed to evaluate the cytotoxic effects of the target compound, utilizing different concentrations ranging from 0–100 μ g/mL. The results were expressed as growth inhibitory concentration (IC₅₀ μ g/mL) values, where the necessitated concentration produced a 50% inhibition of cell growth after 24 h of incubation in assessment with the untreated cell control as shown in Table 1.

Table 1. IC₅₀ values (μ g/mL) of the target compound **4** against MCF-7, HCT-116, PC-3, A549, and HepG-2 cell lines.

Compound	IC ₅₀ μ g/mL ^a						
	Cancerotoxicity			Normotoxicity			
	MCF-7	HCT-116	PC-3	A549	HepG-2	HFL-1	WI-38
4	11.6 \pm 0.11 ^b	18.1 \pm 0.19 ^b	2.4 \pm 0.1	3.2 \pm 0.1	10 \pm 0.01 ^b	25.5 \pm	24.5 \pm
Vinblastine	6.1 \pm 0.05	2.6 \pm 0.01	2.3 \pm 0.1	3.78 \pm 0.01	4.6 \pm 0.08	0.3324.1 \pm 0.1	1.3221.7 \pm 1.2
Colchicine	17.7 \pm 0.12	42.8 \pm 0.2	9.6 \pm 0.1	21.3 \pm 0.03	10.6 \pm 0.4	-	-

^a IC₅₀ values are expressed in μ g/mL as mean values of triplicate wells from at least three experiments and are reported as the mean \pm standard error. ^b [52].

From Table 1, it is evident that the halogenated 2-amino-4-(2,3-dichlorophenyl)-6-methoxy-4*H*-benzo[*h*]chromene-3-carbonitrile (**4**) displayed excellent to modest growth inhibitory activity against the tested tumor cell lines and weak activity against the normal cell lines. The assessment of the compound's cytotoxicity against the cancer cell lines MCF-7, HCT-116, PC-3, A549, and HepG-2 indicated that compound **4** (IC₅₀ = 2.4 \pm 0.1 and 3.2 \pm 0.1 μ g/mL) is potent against PC-3 and A549 in comparison with Vinblastine and Colchicine (IC₅₀ = 2.3 \pm 0.1, 3.78 \pm 0.01, 9.6 \pm 0.1 and 21.3 \pm 0.03 μ g/mL), respectively. Additionally, molecule **4** exhibited more potency and efficacy in evaluation with Colchicine (IC₅₀ = 17.7 \pm 0.12, 42.8 \pm 0.2, 17.7 \pm 0.12 and 10.6 \pm 0.4 μ g/mL) against MCF-7, HCT-116, and HepG-2 cancer cell lines (IC₅₀ = 11.6 \pm 0.11, 18.1 \pm 0.19 and 10 \pm 0.01 μ g/mL), respectively.

2.3.2. In Vitro EGFR and VEGFR-2 Inhibition

The regulation of cell proliferation, growth, and apoptosis are mediated through several signal transduction cascades by the epidermal growth factor receptor (EGFR), which is a tyrosine kinase transmembrane receptor [53]. Moreover, the EGFR-signaling pathways stimulate the vascular endothelial growth factor VEGF-2, which is considered the key inducer of tumor angiogenesis [54]. Therefore, the examined target compound **4** was assessed for its inhibitory behavior against EGFR and VEGFR-2, employing a kinase assay kit that detects the amount of adenosine triphosphate (ATP) remaining in the kinase reaction solution [55] and deriving a comparison to the inhibition of the reference protein

kinases inhibitor Sorafenib as illustrated in Table 2. Compound 4 exhibited comparable inhibitory activity on EGFR (IC_{50} value $0.2162 \pm 1.1 \mu\text{M}$), which was 0.9-fold the activity of Sorafenib (IC_{50} value $0.2307 \pm 1.8 \mu\text{M}$). In the case of VEGFR-2, the IC_{50} value for compound 4 and Sorafenib was 0.2592 ± 1.5 and $0.3075 \pm 1.2 \mu\text{M}$, which was 0.8-fold the value of Sorafenib and exhibited the highest inhibitory effect on the catalytic activity of EGFR/VEGFR-2, as shown in Table 2.

Table 2. EGFR and VEGFR-2 inhibitory activities of compound 4 with their fold inactivation relative to the Sorafenib.

Compound	EGFR		VEGFR-2	
	IC_{50} (μM)	Fold to Sorafenib	IC_{50} (μM)	Fold to Sorafenib
4	0.2162 ± 1.1	0.9	0.2592 ± 1.5	0.8
Sorafenib	0.2307 ± 1.8	1.0	0.3075 ± 1.2	1.0

EGFR: epidermal growth factor receptor; VEGFR-2: vascular endothelial growth factor receptor 2.

2.4. Molecular Crystal Description for Compound 4

The crystallographic structure of molecule 4 revealed lattice parameters area: $a = 7.8561(4) \text{ \AA}$, $b = 9.2701(5) \text{ \AA}$, $c = 12.8343(7) \text{ \AA}$, $\beta = 89.852(4)^\circ$. The molecule is composed of three fused rings, which are exactly aligned with each other (Figure 1). The dichlorophenyl ring is located outside of the planarity for the three fused rings by 1.52 \AA (Table S1). Furthermore, the dichlorophenyl fragment plane deviates by 119.41 from the mean plane (through the pyran ring), indicating that the dichlorophenyl ring is perpendicular to the pyran moiety. The molecular conformation structure was stabilized through the soft intramolecular interaction $\text{Cl1} \cdots \text{H1}$, which serves to determine the rotation of the dichlorophenyl and $4H$ -benzo[*h*]chromene groups (Figures S8 and S9). Moreover, $\text{OC-H} \cdots \text{Cl}$ and $\text{N-H} \cdots \text{NC}$ H-interactions formulate the ribbons that form throughout the length of the *a*-axis. These ribbons are linked in a stepped pattern through $\text{C-H} \cdots \text{N}$, as they are parallel to each other (Figure S10).

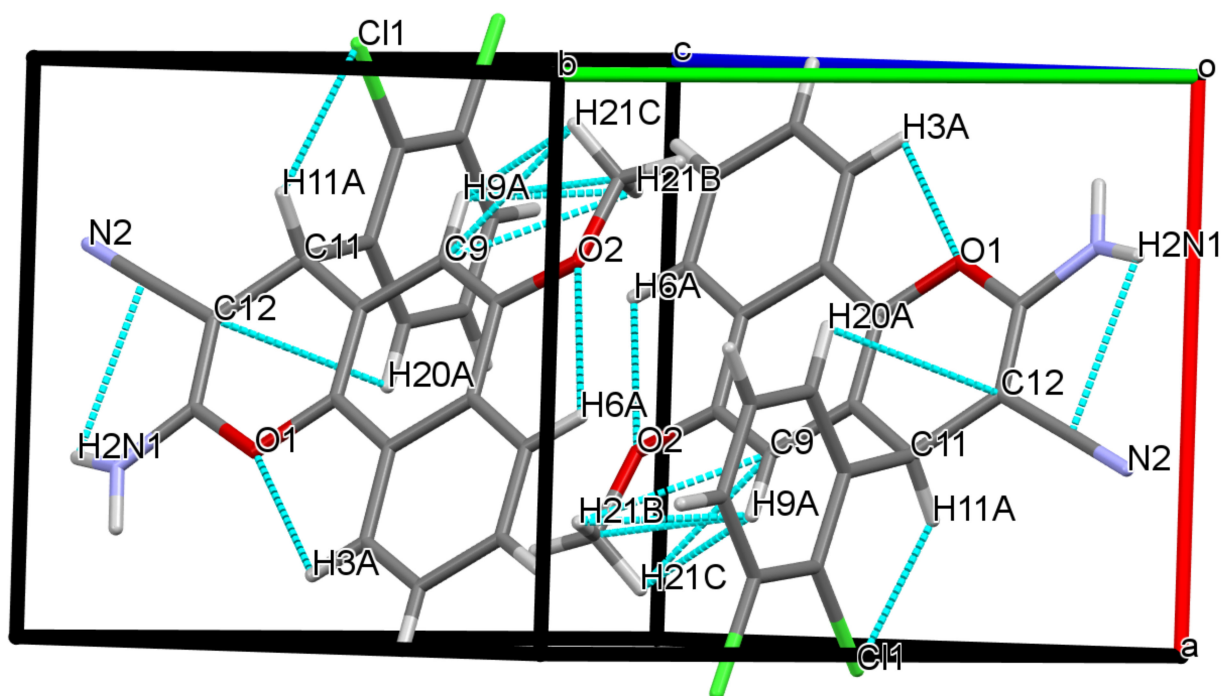


Figure 1. The H-bonded chain viewed along the *b*-axis direction. $\text{OC-H} \cdots \text{Cl}$ and $\text{N-H} \cdots \text{NC}$ are represented in blue dashed lines.

The torsion angle between the plane of the C11-C15 in the dichlorophenyl ring group and that of the pyran moiety defined by C12/C11/C15/C20 is 55.8 (5)°. The rotational orientation of the amino fragment is located in a portion of the intramolecular C11-H11A•••C11 H-bond (Table 3 and Figure 1). C14-C12-C13-N1 has a torsion angle of 177.56 (1)° that indicates that the NH2 moiety is switched substantially out of the plane. In the crystal package, N1-H2•••N2 and C21-H21A•••C11 H-bonds (Table 3) generate ribbons, growing along the b-axis direction (Figure 1). As these are generated by the 21 axis, both N2-H2•••N1 H-bonds are fairly wide and bind the two particles together. The three dimensions for the crystal packaging can be defined by arranging the narrow layers that are parallel to each other (Figure S10).

Table 3. The H-bond geometry of compound 4 (Å, °).

D—H A	D—H	H A	D A	D—H A
C11—H11 N2 ⁱ	0.416 (19)	2.54 (19)	2.939 (14)	110(5)
C9—H21 H9A ⁱⁱ	0.136 (18)	2.764 (18)	2.311 (19)	119 (4)
N2—H2N1C14O2 ⁱ	0.546 (2)	2.204 (19)	2.649 (16)	135.5 (6)

Symmetry codes: (i) $x + 1, y + 1/2, -z + 3/2$; (ii) $-x, -y + 1/2, z - 1/2$.

The results in Table S1 demonstrated a strong relationship between the theoretical and experimental results. The DFT values, achieved in the gas phase, exhibited little deviation in appraisal with the experimental data, which is due to the intermolecular interactions not being taken into account in the DFT simulation. The optimization geometry for the O4-C36, C11-C28 and N5-C26 bond lengths in compound 4 for both data were discovered to be 1.378, 1.728, 1.146, and 1.3941 (18) Å for XRD and 1.378, 1.727 and 1.147 Å for DFT. The bond angle and length values of derivative 4 are in close agreement with a correlation coefficient (0.98 and 0.99, respectively (Table S1)), which were calculated using DFT and XRD. These results confirm that the DFT simulation yielded optimized molecular structure data approximate to that obtained through the XRD analysis. As a result and in light of the DFT simulation, the electronic characteristics may be explored for compound 4.

2.4.1. The Hirschfield Analysis of Molecular Packing

The Hirschfield “HF” surfaces and all the patterns of the intermolecular bonds, which contribute to the molecular packing of derivative 4, are mapped in Figure 2. The quantified $dnorm$ was written as $(dnorm = (di - rodWi)/rodWi + (de - rodWe)/rodWe)$ [56], where $rodWi$ and $rodWe$ are connected to Vander-Waals radii, which measure how close the interior and outer particles are to each other in terms of morphology. Short $rodW$ submits to the positive $dnorm$, while long $rodW$ has a negative value. Crystal Explorer [57] was applied to obtain a link between de and di of the HFM for compound 4. The 3D HF for compound 4 was plotted in Figure 2 with $dnorm$ in (−0.4616 to 1.5334) Å, di (−0.8272 to 2.7847) Å, de (0.8270–2.8507), shape-index (−1.00 to 1.00) Å, curvedness (−4.00 to 4.00) Å, and patch fragment (0.00–12.00) Å. Molecule 4 is packed with its shortest interactions, which consist of N•••O/O•••N and Cl•••Cl. The O•••H contacts are represented in the $dnorm$ fingerprint as a red area, and these interactions are shorter than the $vdWs'$ radii (Figure 2). In addition, the relatively long O•••H/H•••O (2.3%), C•••O/O•••C (2.5%), and C•••Cl/Cl•••C (3.6%) contacts contributed to the crystal packing. The H•••H are the most dominant, with 31.2% of the whole maps' area. The absence of the major π - π stacking interactions was demonstrated by the absence of red and blue triangles in SI and the high green flat site in curvedness (crv). The crv fingerprint examines the morphology for the particle surface. The flat surface and sharp curvature zones are relevant to the lowest degree of curvedness and the sharp curvedness degree, respectively. Because of the linkages between the neighboring molecules, the surface was divided into two patches. Si is a sensitive indicator for any lattice shape deviation. Red triangles denote the concave zone, which is located on the particle's upper plane and indicates dichlorophenyl outside of the surface. The triangles

with blue highlight demonstrate the phenyl fragment and are localized on the exterior surface. The concluded data from SI agreed with the 2D fingerprint.

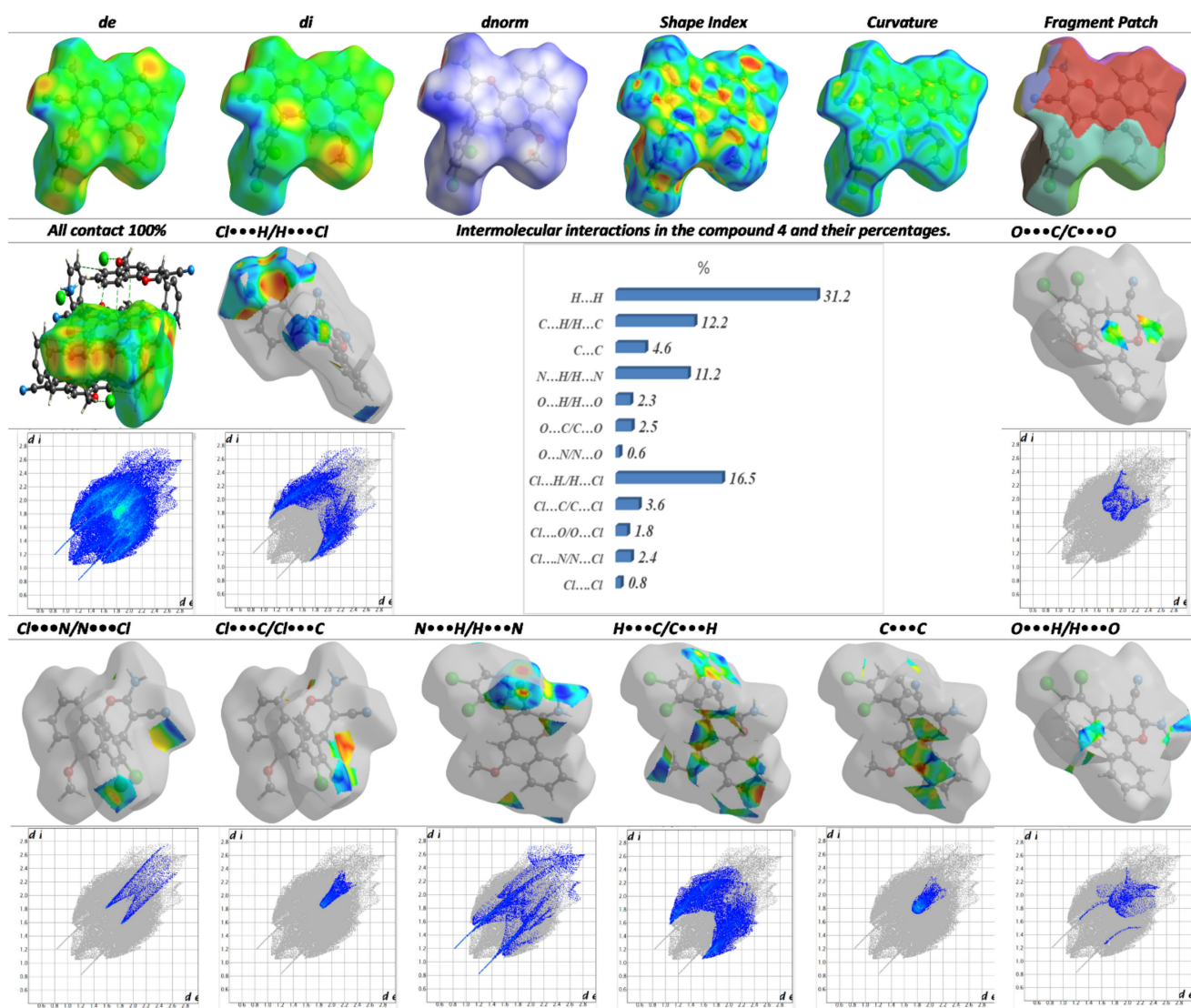


Figure 2. The HFM, represented in 2D interaction diagrams, and its contribution in compound 4 as represented in the d_{norm} , d_i , d_e , shape index “si”, curvedness “cro”, and fragment batch “fb”.

2.4.2. Analysis of the Quantum Theory of Atoms in Molecule “QTAIM”

QTAIM is a beneficial analysis of the H-interaction [56], utilizing quantum mechanics that describe the atom as an open shell system. As postulated [57], NCI can be analyzed depending on the electron density (ρ_c) and Laplacian electron density ($\nabla^2\rho_c$) at the bond critical point (BCP) between a pair of atoms in the molecule and a critical point for the ring (RCB). The characteristics of the electronic energy densities at these BCPs can be used to classify and describe interactions between a chemical bond (ionic, metallic, covalent, etc.). For all BCPs, we also derived the ellipticity (ϵ) (Table S2). The optimization of compound 4, gained from the QTAIM analyses, includes the atomic basin path, BCP, and the RCP isoSurface, as represented in Figure 3.

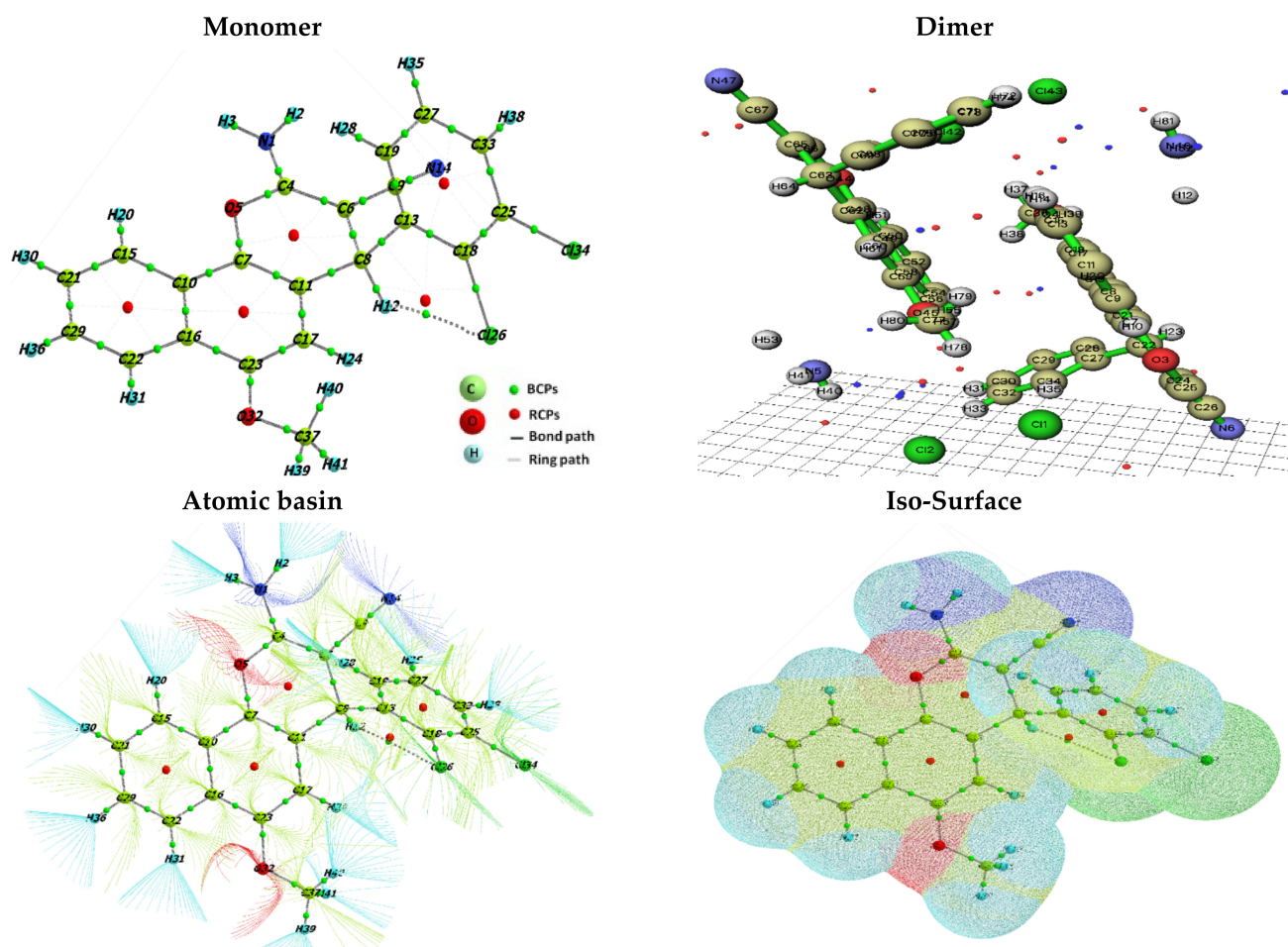


Figure 3. QTAIM molecular graph based on non-covalent interactions.

The ρ_c and $\nabla^2\rho_c$ for the strong H-bond at BCP should be within 0.002 and 0.034 a.u. and 0.024–0.139 a.u. The shared and closed shell interactions are represented by ($\rho(r) \geq 0.14$ a.u. and $\nabla^2\rho(r) < 0$ a.u.) and ($\rho(r) \leq 0.05$ a.u. and $\nabla^2\rho(r) > 0$), respectively [58]. Compound 4 displayed a ρ_c range of 0.014 to 0.403 a.u. and a negative value for $\nabla^2\rho(r)$, which suggested that the presented H-interaction is a shared-shell type (Table S2). Furthermore, the $\nabla^2\rho(r)$ system was employed to further classify the H-bond interactions, such as (i) the strong H-bonds with a covalent nature with $\nabla^2\rho(r) < 0$ and (ii) the partial covalent (intermediate H-bonds) with $\nabla^2\rho(r) > 0$ (iii) $\nabla^2\rho(r) > 0$ for the weak H-bonds, electrostatic and non-covalent character [58]. The two strong H-bonds with a covalent nature were confirmed by the positive value for $\nabla^2\rho(r)$ for the Cl26•••H12 and O1•••H29 BCPs. Additionally, there was one weak H-bond interaction (N1•••H3) with a negative $\nabla^2\rho(r)$, which supported this interaction as a noncovalent bond (Table S2).

2.4.3. Weak Interaction Profile Non-Covalent Interactions (NCI)

The NCI is reliant on the nature of the covalent bond (degree of electron sharing), but the obvious variation between the aforementioned two types involves the electromagnetic interactions between molecules or within a molecule. The NCI performs a vital role in the 3D arrangement of super-molecules such as proteins and nucleic acids that are bound to each other by the NCI. Furthermore, NCI has a strong influence on crystallinity, material design, drug design, and self-assembly. Graphs between the energy via the reduced density gradient (RDG) for compound 4 are described in Figure 4. The strong H-bonds in compound 4 have negative energy (−0.04 to −0.100 a.u.), attributed to the Cl•••H

interaction. The energy in the range from -0.1 to 0.1 a.u. is referred to Vander-Waals attraction (weak hydrogen bonds) of $N_2 \cdots H_2$ in **4**. In this case, the strong repulsive force (steric force) occurred in the range from 0.050 to 0.01 a.u. between the dichlorophenyl and pyran moieties.

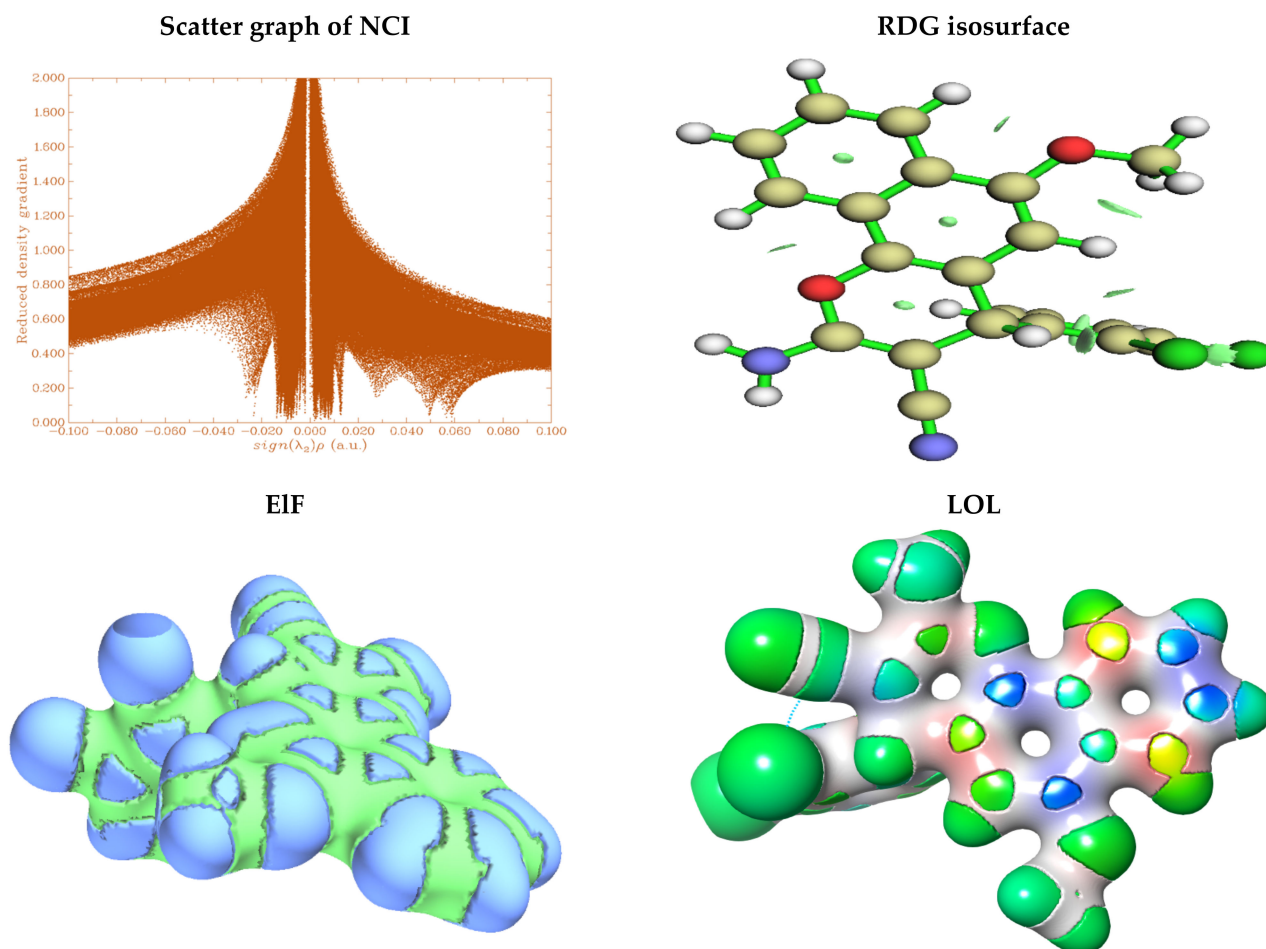


Figure 4. Different weak interaction types for compound **4**.

The Reduced Density Gradient (RDG)

The RDG was directly proportionated with the electronic cloud for the particles, and they are mapped in Figure 4. The molecule with the highest RDG electronic density is represented in green and red colors. The orange and red areas exhibit high electronically reduced density in the range of 0.9000 – 1.000 . The orange regions are distributed around all the skeletons of compound **4**. The moderate RDG, displayed in green color with a range of values from 0.500 to 0.800 , depicts nitrogen and chlorine atoms. The low RDG with blue color is condensed over oxygen atoms for molecule **4**.

LOL (Localized Orbit Locator) and ELF (Electron Localization Function) Profiles

The ELF and LOL were incorporated to study the electrical and geometric structure relation and to obtain a better understanding of the bond mechanics of the particles. In this paper, ELF and LOL analyses were utilized to investigate the topological properties of monomer **4** in the aqueous phase. In Figure 4, green signifies a zone with high ELF and LOL values while blue shows a region with low ELF and LOL values. The red and blue colors indicate electron localization and delocalization [59]. Accordingly, the blue area within these graphs portrays the localization of electron depletion around the H atoms of the aromatic rings. Meanwhile, the green sectors (electron rich) have been capped over

the carbon of the benzopyran moiety. The blue over the pyran ring indicates the highest delocalization zone. The electron-rich sites with corresponding H-bond donor atoms of monomers are influenced to produce H-bonds, which subsequently form dimer structures.

2.5. Reactivity Profile Based on Analysis of Frontier Orbitals, AEPM and ALIEM Surfaces

The objective of this section is the identification of the global reactivity (GR) of molecule 4, which is conducted utilizing FMO [60]. Bultinck et al. [61] postulated that “the energies of the highest occupied molecular orbital and the lowest unoccupied molecular orbital (HOMO and LUMO energies) belong to the most popular quantum chemical descriptors”. The HOMO examines the site ability to contribute electrons, while the LUMO describes the electron acceptor area [60]. The HOMO and LUMO maps indicate the distribution of the orbitals in 3D in Figure 5. It is displayed that the distribution of the HOMO and LUMO shifted over the benzopyran moiety, meaning that the benzopyran moiety has high electron donating ability and accepting features following the cyclo-condensation reaction. As expected, the benzopyran moiety correspondingly experiences high reactivity [58].

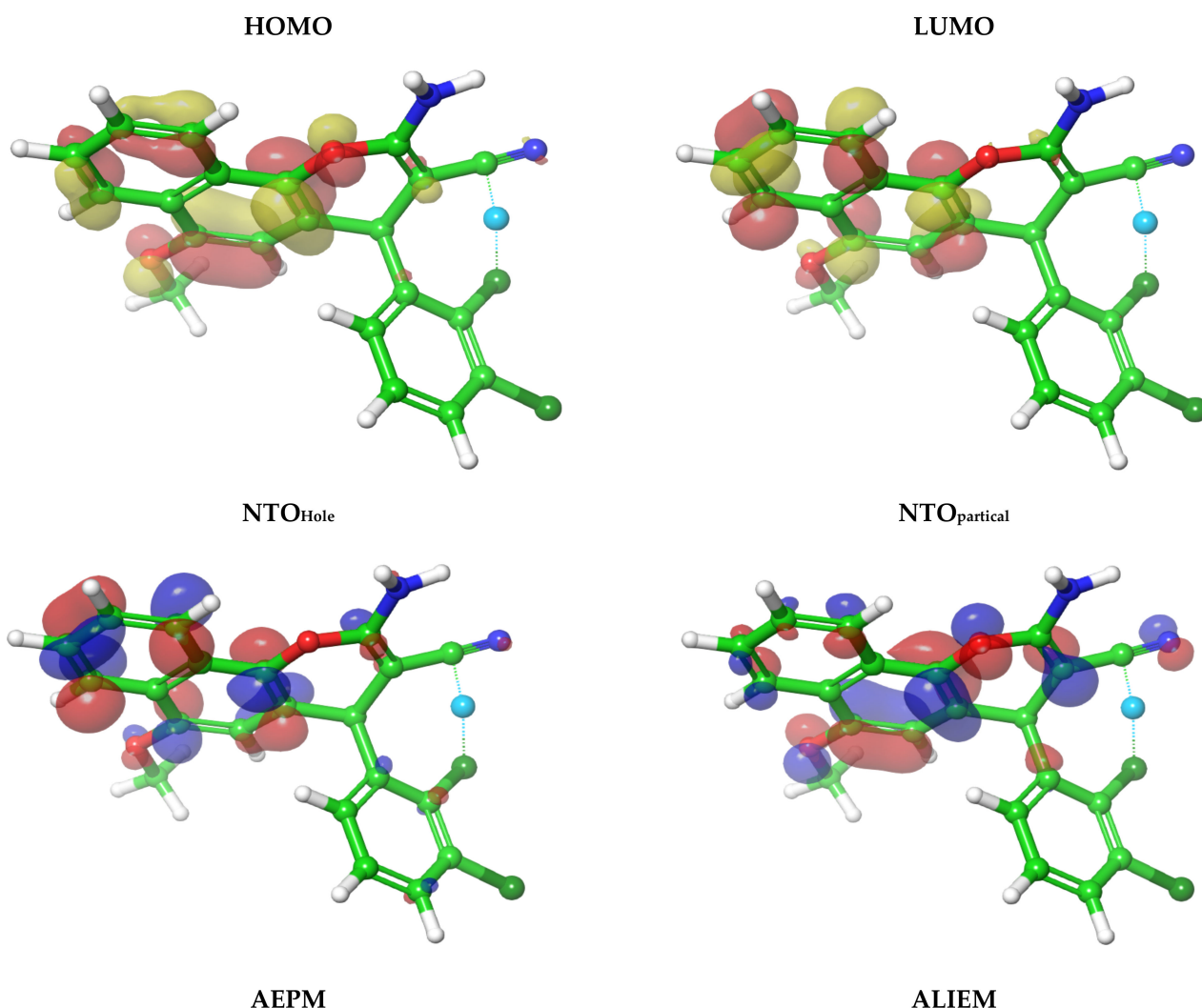


Figure 5. Cont.

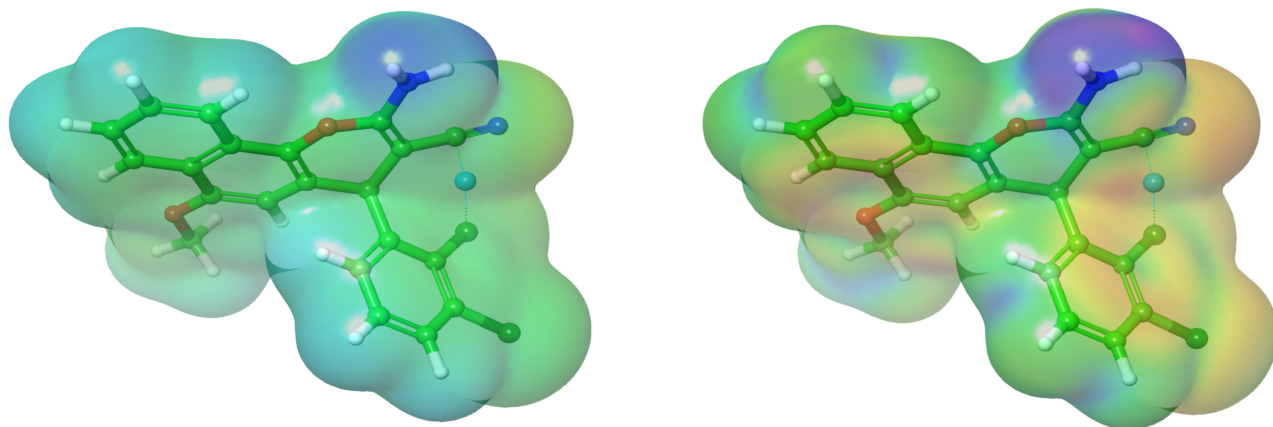


Figure 5. FMO included HOMO and LUMO, AEPM and ALIE for molecule 4.

The different GR parameters were calculated and are listed in Table 4, including: η (hardness), S (softness), χ (electronegativity), ωi (electrophilicity index), ε (nucleophilicity index), I (ionization potential), A (electron affinity), and ΔN_{max} (transfer of a maximum amount of electrons). The energy gap (ΔG) indicates the stability and reactivity index, and the small ΔG particles are likely to have limited stability alongside high reactivity and vice versa if ΔG is higher [62].

Table 4. Calculated chemical reactivity for compound 4 at the DFT/B3LYP/6-311**G (d,p) basics sets.

HOMO	LUMO	ΔG	η	S	χ	ωi	ε	I	A
−0.203	−0.050	0.154	0.077	13.023	−0.127	0.104	9.580	0.203	0.050
$ALIEM_{min}$	$ALIEM_{max}$	$\Delta E_{Back-donation}$	ΔN_{max}						
261	375	−0.019	−0.824						

$$= \frac{1}{2 \left[\frac{\partial^2 E}{\partial^2 N^2} \right]_{v(r)}}, S = \frac{1}{\eta}, \chi = - \left[\frac{\partial E}{\partial N} \right]_{v(r)}, \omega i = \frac{\mu^2}{2\eta}, \varepsilon = \frac{1}{\omega i}, \Delta N_{max} = \frac{\chi}{2\eta}, \Delta E_{Back-donation} = \eta/4 \quad (1)$$

The calculated HOMO/LUMO values are −0.203 and −0.049 a.u. The small $\Delta G = 0.153$ a.u. confirms the identity of molecule 4 as a soft molecule ($S = 13.02$ a.u.) with low kinetic stability. It is evident that the increase within the ε value in assessment with the ωi value of derivative 4 subsequently increases its nucleophilic attack ability against the biological receptors. The $\Delta E_{Back-donation}$ (energy back donation) term refers to the amount of electrons transferred from the receptor to inhibitor. The small $\Delta E_{Back-donation} = -0.0192$ value revealed a high interaction ability with biological systems. Furthermore, the high amount of electron cloud transfer from compound 4 to a biological system ($\Delta N_{max} = 3.2$ a.u.) further substantiates the results via the high inhibition efficacy. Moreover, the NTOs formalisms have been studied as compared to the standard canonical molecular orbital. Through the introduction of a lower number of relevant orbitals in evaluation with the standard assays, the NTOs present a clearer insight into the orbitals responsible for binding with the receptor, which is illustrated in Figure 6. The plotted NTO pair reflects the importance of the excitation state in biological media. Based on our previous study [63], it is possible to assert that the intramolecular charge transfer transpires over the benzochromene skeleton.

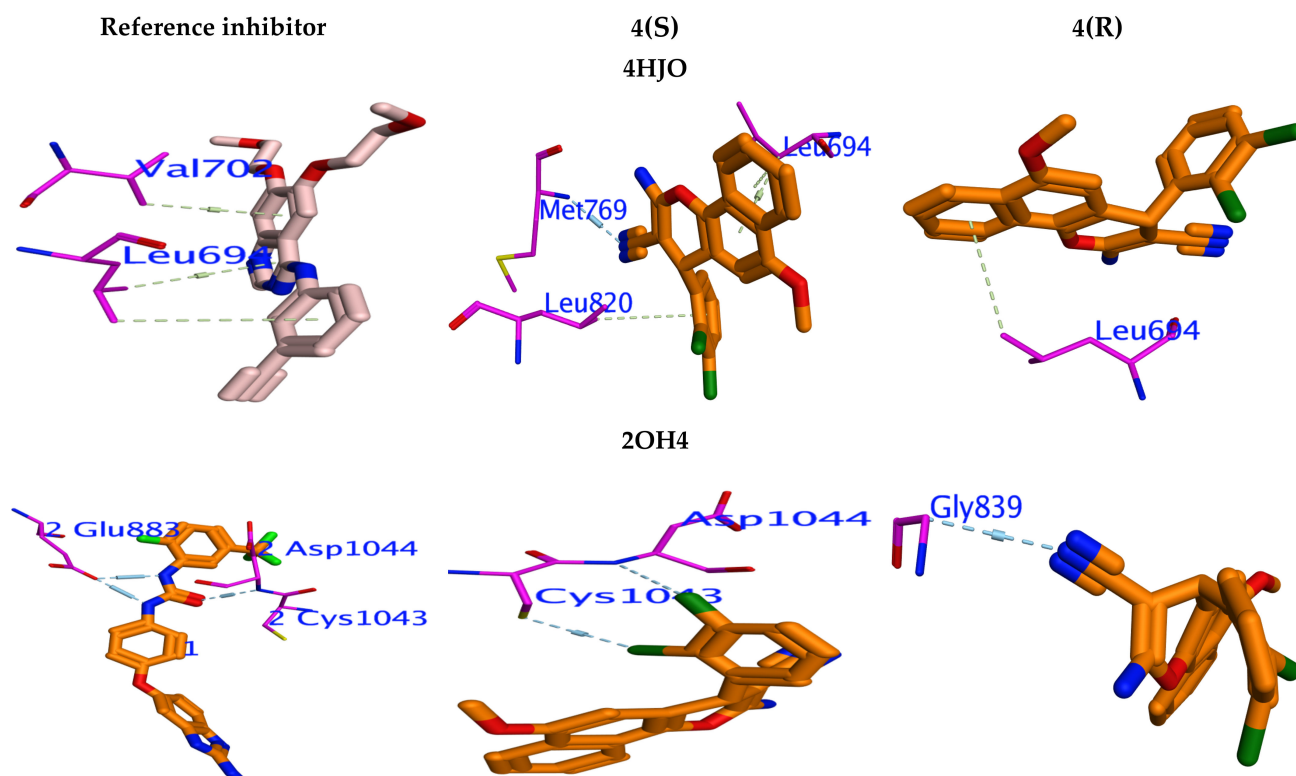


Figure 6. Binding approach of stereoisomers for compound **4** and reference inhibitors into 4HJO and 2OH4. H-bonds are represented with blue lines.

The average electrostatic potential map (AEPM) and average local ionization energy map (ALIEM) are portrayed in Figure 5, which express the impact of the electrophilic and nucleophilic assaults on the sensitivity of molecular sites [64]. The AEPM was initially used to examine the distribution of electrons along reactive particle sites and subsequently calculate the interaction and physicochemical behaviors [65]. Additionally, the AEPM introduces a dynamic through repulsive and attractive interactions. A green cave was envisaged for an intermediate potential value. The fluctuations of colors on AEPM demonstrate the variation in the electrostatic potential. The highest green area is shielded over the benzo[*f*]chromene moiety, while the blue region is localized over the amine moiety. The color variation denotes a helpful recognition of how the investigated particle sites cleverly form intermolecular interactions as well as where the highest insightful locations are experienced by electrophilic and nucleophilic attacks. The growing blue zone is due to a high electrophilic ability, which is considered as a substrate to distinguish the binding site through the substrate \rightarrow receptor electrostatic force. In order to predict the favorable molecular sites for the electrophilic attacks, ALIEM is preferable to AEPM [64]. This fingerprint depicts the locations, where electrons are loosely bonded and hence are more easily removed (the sites that are most sensitive to electrophiles). ALIEM is represented equation-wise by Sjöberg [65] as a sum of orbitals weighted by $I(r) = \sum_i \frac{p_i(\vec{r})|\epsilon_i|}{p(\vec{r})}$, where $p_i(\vec{r})$ is the electronic cloud for the orbital (*i*) at the exact point (\vec{r}) , $|\epsilon_i|$ is the energy orbital, and $p(\vec{r})$ reflects the summation electronic density function. The red color of ALIEM indicates that the highest electron density is bounded strongly in the vicinity of the methoxy group. Moreover, the electron density suffers from low distribution around the molecular skeleton. In addition, the ALIEM energy in Table 4 reflects the lowest amount of energy required in order to separate the electron. Molecule **4** is more favorable to nucleophilic attacks due to the high ability to attract electrons.

2.6. The Molecular Docking Profile

The molecular docking analysis has been achieved to explain the potency for the promising molecule **4** in vitro against the EGFR and VEGFR-2 kinases by deciphering their probable means of interaction with PDB: 4HJO [66] and PDB:2OH4 [66]. Glide's module has been employed to perform docking analysis, which was validated by the redocking of the original inhibitors (Erlotinib and Benzimidazole) into the crystal structures of EGFR and VEGFR-2. The free-binding energies (ΔE) are displayed in Table 5. The original inhibitors and molecule **4** have been suitably fitted into the desired binding sites for the tested crystal structures. The adenine pocket of EGFR and VEGFR-2 was targeted by the hetero ring for Erlotinib and Benzimidazole, which formed an identical H-bond with Met769, Thr766, and Gln767. Moreover, compound **4** docked fruitfully into the active sites in the same manner as the original inhibitors. From Table 5, molecule **4** displayed promising binding affinities in appraisal with the reference inhibitors for all the investigated kinases.

Table 5. The binding affinity for compound **4** with docking score (kcal/mol) against EGFR and VEGFR-2.

	ΔE	rmsd	H.B	EInt.	E_ele		ΔG	rmsd	H.B	Int.	E_ele
	4HJO						2OH4				
4(S)	−6.73	1.34	−6.17	−21.57	−8.28	4(S)	−6.96	0.87	13.81	−24.05	−6.33
Erlotinib	−5.36	1.34	−8.17	−17.97	−9.20	Benzi— midazole	−6.96	1.44	−36.17	−15.97	−6.20

ΔG : free binding energy of the ligand, EInt.: binding affinity of H-bond interaction with receptor, H.B.: H-bond energy between protein and ligand. Eele: electrostatic interaction over the receptor.

In EGFR (PDB:4HJO), molecule **4(S)** has a higher binding affinity ($\Delta E = -6.73$ kcal/mol) in evaluation with **4(R)** ($\Delta E = -5.83$ kcal/mol), which explicates the promising potency ($IC_{50} = 0.2162 \mu M$) for **4(S)**. Furthermore, compound **4(S)** possesses more hydrogen interactions with the amino acid backbone Met769 and vital π - π stack bond upon Leu694 and leu820 (Figure 6). Conversely, derivative **4(R)** retains a weak stack interaction with Leu694. In VEGFR-2 (PDB:2OH4), the established molecule **4(S)** disclosed nearly the same binding affinity to the VEGFR-2 inhibitor with $\Delta E = -6.96$ kcal/mol, which corresponded to approximately the same $IC_{50} = 0.2592 \mu M$. This compound was encased within the binding pocket in the same manner as the original inhibitor through its arrangement in a parallel mode with the circular Asp1044 and Cys1043 amino acids, inciting important H-bonds with compound **4** (Figure 6). Lastly, molecule **4(S)** displayed only one weak H-bond with Gly839 ($\Delta E = -5.48$ kcal/mol).

3. Experimental Section

3.1. Materials and Equipment's

All chemicals purchased and instruments used are mentioned in the Supplementary Material.

3.2. Synthesis of 2-Amino-4-(2,3-Dichlorophenyl)-6-Methoxy-4H-Benzo[h]chromene-3-Carbonitrile (**4**)

Prepared as previously reported [52] (see Supplementary Materials).

3.3. Biological Screening

Cell culture, cytotoxicity evaluation using viability assay and in vitro tyrosine kinases inhibition are mentioned in Supplementary Materials.

3.4. X-ray Crystallography Analysis

The slow evaporation technique was applied to obtain 4 single crystals with CCDC 2054708. The other procedures are mentioned in Supplementary Material Section 3.4. [67,68].

The crystallographic data and refinement information are summarized in Table S3 and Figure 7.

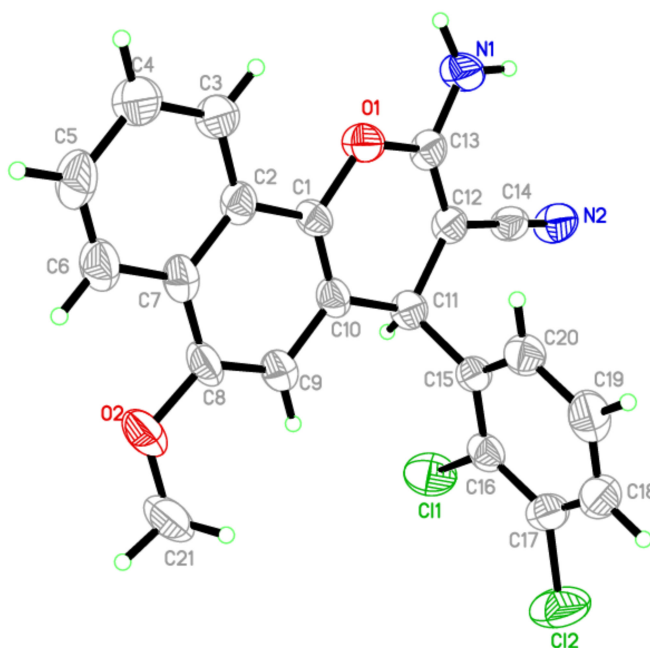


Figure 7. Crystal structure for compound 4.

3.5. Hirschfeld Map Analysis

Crystal-Explorer [69] was used to build the 2D and 3D HFMs. To explicate, the crystallographic data for 4 were imported into TONTO, which were implemented in Crystal Explorer.

3.6. Quantum Chemical Calculations

The DFT theory was used for all computations and optimization geometry using the “Becke3-Lee-Yang-parr; B3LYP” with “6-311**G (d,p)” basis set [70].

3.7. The Molecular Docking

The 3D crystal structure for both EGFR and VEGFR-2 kinases was generated by Glide-tool as described [71]. All docking steps were carried out by ordinary method of Maestro.

4. Conclusions

In conclusion, microwave irradiation was utilized for the preparation of compound 4, which originates in crystal form and which was characterized by X-ray diffraction. Compound 4 was evaluated *in vitro* for its anti-proliferative efficacy against cancer cell lines MCF-7, HCT-116, PC-3, A549, and HepG-2. Furthermore, it was evaluated over the two normal cell lines (human fetal lung “HFL-1” and human diploid fibroblasts “WI-38”) and demonstrated promising and healthy selective cytotoxicity against the malignant cell lines and revealed weak behavior against the normal cell lines. Conversely, compound 4 exhibited potent inhibition against the EGFR and VEGFR-2 kinases, which are superior in evaluation with the inhibitory activity of the reference drug Sorafenib. The molecular docking analysis for both stereoisomers in compound 4 over the active sites of EGFR and VEGFR-2 kinases provides to us a reasonable explanation of the biological result for 4(S) over 4(R).

Supplementary Materials: The following are available online at <https://www.mdpi.com/article/10.3390/cryst12050737/s1>, Figure S1: ¹H NMR of compound 4, Figure S2: ¹H NMR 8–6 ppm of compound 4, Figure S3: ¹³C NMR of compound 4, Figure S4: ¹³C NMR-DPT 45 of compound 4, Figure S5: ¹³C NMR-DPT 90 of compound 4, Figure S6: ¹³C NMR-DPT 135 of compound 4, Figure S7: ¹³C NMR-APT of compound 4, Figure S8: The number of atoms for compound 4 viewed along the a-axis direction, Figure S9: Packing viewed along the b-axis direction with C-H•••N hydrogen bonds shown as light purple dashed lines, Figure S10: Detail of the intermolecular interactions forming one chain viewed along the b-axis direction. N-H•••N and Cl•••H-O hydrogen bonds are shown as blue dashed lines, Table S1: Selected experimental and theoretical geometrical parameters for compound 4, Table S2: Topological parameters at BCP of compound 4 (electron density($\rho(r)$), Laplacian of electron density ($\nabla^2\rho(r)$), ellipticity (ϵ), Hamiltonian form of kinetic energy density ($K(r)$) and distance (D , in Å) of bond path length (BPL) from the nuclear attractors), and compound 4 check CIF file, Table S3: Crystal data and structure refinement parameters for compound 4.

Author Contributions: A.M.E.-A., A.M.F., A.E.-G.E.A., A.M.N., H.M.M., R.M.O. and A.A.A. designed the proposed methods and analyzed the spectral data; A.M.E.-A. performed the experiments and implemented the biological study; A.A.E. performed DFT theoretical calculations; M.Y.A. analyzed the biological data and reviewed and edited the draft. H.A.G. carried out and wrote the X-ray processes. All authors have read and agreed to the published version of the manuscript.

Funding: This work was funded by the Deanship of Scientific Research, King Saud University, through vice Deanship of Scientific Research Chairs.

Institutional Review Board Statement: Not applicable.

Informed Consent Statement: Not applicable.

Data Availability Statement: Not applicable.

Acknowledgments: The authors extend their appreciation to the Deanship of Science Research at King Khalid University, Saudi Arabia for funding this work through General Research Project under Grant Number (RGP.1/245/43).

Conflicts of Interest: The authors declare no conflict of interest.

References

1. Van Kiem, P.; Nhiem, N.X.; Anh, N.H.; Yen, D.T.H.; Cuong, N.T.; Tai, B.H.; Yen, P.H.; Nam, N.H.; Van Minh, C.; Chinh, P.T.; et al. Enantiomeric chromene derivatives with anticancer effects from *Mallotus apelta*. *Bioorganic Chem.* **2020**, *104*, 104268. [[CrossRef](#)] [[PubMed](#)]
2. Park, B.H.; Lee, H.J.; Lee, Y.R. Total Synthesis of Chiricanine A, Arahylin-1, trans-Arachidin-2, trans-Arachidin-3, and Arahylin-5 from Peanut Seeds. *J. Nat. Prod.* **2011**, *74*, 644–649. [[CrossRef](#)] [[PubMed](#)]
3. Sobolev, V.S.; Neff, S.A.; Gloer, J.B. New Stilbenoids from Peanut (*Arachis hypogaea*) Seeds Challenged by an *Aspergillus caelatus* Strain. *J. Agric. Food Chem.* **2008**, *57*, 62–68. [[CrossRef](#)] [[PubMed](#)]
4. Ribeiro, A.B.; Abdelnur, P.V.; Garcia, C.F.; Belini, A.; Severino, V.G.P.; da Silva, M.F.D.G.; Fernandes, J.B.; Vieira, P.C.; de Carvalho, S.A.; de Souza, A.A.; et al. Chemical characterization of *Citrus sinensis* grafted on *C. limonia* and the effect of some isolated compounds on the growth of *Xylella fastidiosa*. *J. Agric. Food Chem.* **2008**, *56*, 7815–7822. [[CrossRef](#)] [[PubMed](#)]
5. Coombes, C.L.; Moody, C.J. First Syntheses of 2, 2-Dimethyl-7-(2'-methylbut-3'-en-2'-yl)-2H-chromen-6-ol and 2-(3'-Methylbut-2'-enyl)-5-(2'-methylbut-3'-en-2'-yl)-1, 4-benzoquinone, Novel Prenylated Quinone Derivatives from the New Zealand Brown Alga *Perithalia capillaris*. *J. Org. Chem.* **2008**, *73*, 6758–6762. [[CrossRef](#)]
6. Chen, S.; Cho, M.; Karlsberg, K.; Zhou, D.; Yuan, Y.C. Biochemical and biological characterization of a novel anti-aromatase coumarin derivative. *J. Biol. Chem.* **2004**, *279*, 48071–48078. [[CrossRef](#)]
7. Lloyd, M.D.; Pederick, R.L.; Natesh, R.; Woo, L.W.L.; Purohit, A.; Reed, M.J.; Acharya, K.R.; Potter, B.V.L. Crystal structure of human carbonic anhydrase II at 1.95 Å resolution in complex with 667-coumate, a novel anti-cancer agent. *Biochem. J.* **2005**, *385*, 715–720. [[CrossRef](#)]
8. Purohit, A.; Woo, L.W.L.; Chander, S.K.; Newman, S.P.; Ireson, C.; Ho, Y.; Grasso, A.; Leese, M.P.; Potter, B.V.L.; Reed, M.J. Steroid sulphatase inhibitors for breast cancer therapy. *J. Steroid Biochem. Mol. Biol.* **2003**, *86*, 423–432. [[CrossRef](#)]
9. Schmitt, F.; Gold, M.; Rothmund, M.; Andronache, I.C.; Biersack, B.; Schobert, R.; Mueller, T. New naphthopyran analogues of LY290181 as potential tumor vascular-disrupting agents. *Eur. J. Med. Chem.* **2018**, *163*, 160–168. [[CrossRef](#)]
10. Kasibhatla, S.; Gourdeau, H.; Meerovitch, K.; Drewe, J.; Reddy, S.; Qiu, L.; Zhang, H.; Bergeron, F.; Bouffard, D.; Yang, Q.; et al. Discovery and mechanism of action of a novel series of apoptosis inducers with potential vascular targeting activity. *Mol. Cancer Ther.* **2004**, *3*, 1365–1374.

11. Kheirollahi, A.; Pordeli, M.; Safavi, M.; Mashkouri, S.; Naimi-Jamal, M.R.; Ardestani, S.K. Cytotoxic and apoptotic effects of synthetic benzochromene derivatives on human cancer cell lines. *Naunyn-Schmiedeberg's Arch. Exp. Pathol. Pharmacol.* **2014**, *387*, 1199–1208. [[CrossRef](#)] [[PubMed](#)]
12. El-Agrody, A.M.; El-Mawgoud, H.K.A.; Fouda, A.M.; Khattab, E.S.A.E.H. Synthesis, in-vitro cytotoxicity of 4H-benzo[h]chromene derivatives and structure–activity relationships of 4-aryl group and 3-, 7-positions. *Chem. Pap.* **2016**, *70*, 1279–1292. [[CrossRef](#)]
13. M Hamed, H.; M Fouda, A.; SAEH Khattab, E.; M El-Agrody, A. Synthesis, molecular properties and evaluation of the antitumor activity of 2-amino-6-methoxy-4H-benzo [h] chromenes, 6-methoxy-2-oxo-2Hbenzo [h] chromene. *Curr. Bioact. Compd.* **2017**, *13*, 356–369. [[CrossRef](#)]
14. El-Agrody, A.M.; Fouda, A.M.; Khattab, E.S.A.E.H. Halogenated 2-amino-4H-benzo[h]chromene derivatives as antitumor agents and the relationship between lipophilicity and antitumor activity. *Med. Chem. Res.* **2017**, *26*, 691–700. [[CrossRef](#)]
15. Halawa, A.H.; Elaasser, M.M.; El Kerdawy, A.M.; El-Hady, A.M.A.I.A.; Emam, H.A.; El-Agrody, A.M. Anticancer activities, molecular docking and structure–activity relationship of novel synthesized 4H-chromene, and 5H-chromeno[2,3-d]pyrimidine candidates. *Med. Chem. Res.* **2017**, *26*, 2624–2638. [[CrossRef](#)]
16. Halawa, A.H.; Fouda, A.M.; Al-Dies, A.A.M.; El-Agrody, A.M. Synthesis, Biological Evaluation and Molecular Docking Studies of 4Hbenzo [h] chromenes, 7H-benzo [h] chromeno [2, 3-d] pyrimidines as Antitumor Agents. *Lett. Drug Des. Discov.* **2016**, *13*, 77–88. [[CrossRef](#)]
17. Alblewi, F.F.; Okasha, R.M.; Eskandrani, A.A.; Afifi, T.H.; Mohamed, H.M.; Halawa, A.H.; Fouda, A.M.; Al-Dies, A.-A.M.; Mora, A.; El-Agrody, A.M. Design and synthesis of novel heterocyclic-based 4h-benzo [h] chromene moieties: Targeting antitumor caspase 3/7 activities and cell cycle analysis. *Molecules* **2019**, *24*, 1060. [[CrossRef](#)]
18. Ahmed, H.E.A.; El-Nassag, M.A.A.; Hassan, A.; Okasha, R.M.; Ihmaid, S.; Fouda, A.M.; Afifi, T.H.; Aljuhani, A.; El-Agrody, A.M. Introducing novel potent anticancer agents of 1H-benzo[f]chromene scaffolds, targeting c-Src kinase enzyme with MDA-MB-231 cell line anti-invasion effect. *J. Enzym. Inhib. Med. Chem.* **2018**, *33*, 1074–1088. [[CrossRef](#)]
19. Ahagh, M.H.; Dehghan, G.; Mehdipour, M.; Teimuri-Mofrad, R.; Payami, E.; Sheibani, N.; Ghaffari, M.; Asadi, M. Synthesis, characterization, anti-proliferative properties and DNA binding of benzochromene derivatives: Increased Bax/Bcl-2 ratio and caspase-dependent apoptosis in colorectal cancer cell line. *Bioorganic Chem.* **2019**, *93*, 103329. [[CrossRef](#)]
20. Fouda, A.M.; Okasha, R.M.; Alblewi, F.F.; Mora, A.; Afifi, T.H.; El-Agrody, A.M. A proficient microwave synthesis with structure elucidation and the exploitation of the biological behavior of the newly halogenated 3-amino-1H-benzo[f]chromene molecules, targeting dual inhibition of topoisomerase II and microtubules. *Bioorganic Chem.* **2020**, *95*, 103549. [[CrossRef](#)]
21. Fouda, A.M.; Assiri, M.A.; Mora, A.; Ali, T.E.; Afifi, T.H.; El-Agrody, A.M. Microwave synthesis of novel halogenated β -enamionitriles linked 9-bromo-1H-benzo[f]chromene moieties: Induces cell cycle arrest and apoptosis in human cancer cells via dual inhibition of topoisomerase I and II. *Bioorganic Chem.* **2019**, *93*, 103289. [[CrossRef](#)]
22. Okasha, R.M.; AlBalawi, F.F.; Afifi, T.H.; Fouda, A.M.; Al-Dies, A.-A.M.; El-Agrody, A.M.; Al-Dies, A.-A. Structural Characterization and Antimicrobial Activities of 7H-Benzo[h]chromeno[2,3-d]pyrimidine and 14H-Benzo[h]chromeno[3,2-e][1,2,4]triazolo[1,5-c] pyrimidine Derivatives. *Molecules* **2016**, *21*, 1450. [[CrossRef](#)] [[PubMed](#)]
23. Abd El-Mawgoud, H.K.; Radwan, H.A.M.; El-Mariah, F.; El-Agrody, A.M. Synthesis, Characterization, Biological Activity of Novel 1H-benzo [f]-chromene and 12H-benzo [f] chromeno [2, 3-d] pyrimidine Derivatives. *Lett. Drug Des. Discov.* **2018**, *15*, 857–865. [[CrossRef](#)]
24. Alblewi, F.F.; Okasha, R.M.; Hritani, Z.M.; Mohamed, H.; El-Nassag, M.A.; Halawa, A.H.; Mora, A.; Fouda, A.M.; Assiri, M.A.; Al-Dies, A.-A.M.; et al. Antiproliferative effect, cell cycle arrest and apoptosis generation of novel synthesized anticancer heterocyclic derivatives based 4H-benzo[h]chromene. *Bioorganic Chem.* **2019**, *87*, 560–571. [[CrossRef](#)] [[PubMed](#)]
25. Mohamed, H.; Fouda, A.M.; Khattab, E.S.; El-Agrody, A.; Afifi, T.H. Synthesis, in-vitro cytotoxicity of 1H-benzo[f]chromene derivatives and structure–activity relationships of the 1-aryl group and 9-position. *Z. Für Nat. C* **2017**, *72*, 161–171. [[CrossRef](#)]
26. El-Agrody, A.M.; Fouda, A.M.; Assiri, M.A.; Mora, A.; Ali, T.E.; Alam, M.M.; Alfaifi, M.Y. In vitro anticancer activity of pyrano[3, 2-c]chromene derivatives with both cell cycle arrest and apoptosis induction. *Med. Chem. Res.* **2020**, *29*, 617–629. [[CrossRef](#)]
27. Halawa, A.H.; Elgammal, W.E.; Hassan, S.M.; Hassan, A.H.; Nassar, H.S.; Ebrahim, H.Y.; Mehany, A.B.; El-Agrody, A.M. Synthesis, anticancer evaluation and molecular docking studies of new heterocycles linked to sulfonamide moiety as novel human topoisomerase types I and II poisons. *Bioorganic Chem.* **2020**, *98*, 103725. [[CrossRef](#)]
28. El-Agrody, A.M.; Al-Ghamdi, A.M. Synthesis of certain novel 4H-pyrano [3, 2-h] quinoline derivatives. *Arkivoc* **2011**, *11*, 134–146. [[CrossRef](#)]
29. Al-Sehemi, A.G.; Irfan, A.; El-Agrody, A. Synthesis, characterization and DFT study of 4H-benzo[h]chromene derivatives. *J. Mol. Struct.* **2012**, *1018*, 171–175. [[CrossRef](#)]
30. Sayed, A.Z.; El-Hady, N.A.; El-Agrody, A.M. Condensation of α -cyanocinnamionitriles with 6-bromo-2-naphthol: Synthesis of pyrano [2, 3-d] pyrimidine and pyrano [3, 2-e][1, 2, 4] triazolo [2, 3-c] pyrimidine derivatives. *J. Chem. Res.* **2000**, *2000*, 164–166. [[CrossRef](#)]
31. El-Agrody, A.M.; El-Latif, M.A.; Fakery, A.H.; Bedair, A.H. Heteroaromatization with 4-hydroxycoumarin Part I: Synthesis of some new pyranocoumarins and coumarinopyranopyrimidines. *J. Chem. Res.* **2000**, *2000*, 26–27. [[CrossRef](#)]
32. El-Agrody, A.M.; Al-Dies, A.A.M.; Fouda, A.M. Microwave assisted synthesis of 2-amino-6-methoxy-4H-benzo [h] chromene derivatives. *Eur. J. Chem.* **2014**, *5*, 133–137. [[CrossRef](#)]

33. El-Agrody, A.M.; Khattab, E.S.A.E.H.; Fouda, A.M.; Al-Ghamdi, A.M. Synthesis and antitumor activities of certain novel 2-amino-9-(4-halostyryl)-4H-pyrano[3,2-h]quinoline derivatives. *Med. Chem. Res.* **2012**, *21*, 4200–4213. [[CrossRef](#)]
34. El-Agrody, A.M.; Sabry, N.M.; Motlaq, S.S. Synthesis of some new 2-substituted 12H-chromeno [3, 2-e][1, 2, 4] triazolo [1, 5-c] pyrimidine, 3-ethoxycarbonyl-12H-chromeno [3, 2-e]-[1, 2, 4] triazolo [1, 5-c] pyrimidine-2-one, ethyl 2-formylamino\acetyl-amino-4H-chromene-3-carboxylate and some of their antimicrobial activities. *J. Chem. Res.* **2011**, *35*, 77–83.
35. El-Wahab, A.H.A.; Mohamed, H.; El-Agrody, A.M.; El-Nassag, M.A.; Bedair, A.H. Synthesis and Biological Screening of 4-Benzyl-2H-phthalazine Derivatives. *Pharmaceuticals* **2011**, *4*, 1158–1170. [[CrossRef](#)]
36. Abd-El-Aziz, A.S.; Shipman, P.O.; Neeland, E.G.; Corkery, T.C.; Mohammed, S.; Harvey, P.D.; Mohamed, H.M.; Bedair, A.H.; El-Agrody, A.M.; Aguiar, P.M.; et al. Benzo [f]-and Benzo [h] Coumarin-Containing Poly (methyl methacrylate) s and Poly (methyl methacrylate) s with Pendant Coumarin-Containing Azo Dyes. *Macromol. Chem. Phys.* **2008**, *209*, 84–103. [[CrossRef](#)]
37. Mohamed, H.M.; Abd EL-Wahab, A.H.; El-Agrody, A.M.; Bedair, A.H.; Eid, F.A.; Khafagy, M.M.; Abd-EL-Rehem, K.A. Synthesis and characterization of new diiodocoumarin derivatives with promising antimicrobial activities. *Beilstein J. Org. Chem.* **2011**, *7*, 1688–1696. [[CrossRef](#)]
38. El-Agrody, A.M.; Ali, F.M.; Eid, F.A.; El-Nassag, M.A.A.; El-Sherbeny, G.; Bedair, A.H. Synthesis and Antimicrobial Activity of Thioxopyrimidines and Related Derivatives. *Phosphorus Sulfur Silicon Relat. Elem.* **2006**, *181*, 839–864. [[CrossRef](#)]
39. Al-Dies, A.A.; Amr, A.G.; El-Agrody, A.M.; Chia, T.S.; Fun, H.K. 2-Amino-4-(4-fluorophenyl)-6-methoxy-4H-benzo [h] chromene-3-carbonitrile. *Acta Crystallogr. Sect. E Struct. Rep. Online* **2012**, *68*, o1934–o1935. [[CrossRef](#)]
40. Bedair, A.H.; Aly, F.M.; El-Agrody, A.M.; Eid, F.A.; El-Nassag, M.A.A.; El-Sherbeny, G.M. Preparation and Antimicrobial Activity of *p*-Aminophenylacetic acid Derivatives: Synthesis of Carboxymethylphenylazopyrazoles, (Pyrazolo[3,4-*e*][1,2,4]triazin-2-yl)phenylacetic acid, (1*H*-benzo[*d*]imidazol-2-yl and Oxo-4*H*-benzo[*d*][1,3](oxazin-2-yl)- methylphenyl-isindoline-1,3-dione Derivatives. *Acta Pharm.* **2006**, *56*, 273–284.
41. El-Agrody, A.M.; Hassan, S.M. Activated Nitriles in Heterocyclic Synthesis: Synthesis of Several New 2-Substituted Pyrano[1,2,4]Triazolopyrimidine Derivatives. *J. Chem. Res.* **1995**, 100–101. [[CrossRef](#)]
42. El-Agrody, A.M. Activated nitriles in heterocyclic synthesis: Synthesis of several new naphtho[2,1-*b*] pyran-3-one derivatives. *J. Chem. Res. Synop.* **1994**, 50–51. [[CrossRef](#)]
43. Omar, A.M.; Bajorath, J.; Ihmaid, S.; Mohamed, H.M.; El-Agrody, A.M.; Mora, A.; El-Araby, M.E.; Ahmed, H.E.A. Novel molecular discovery of promising amidine-based thiazole analogues as potent dual Matrix Metalloproteinase-2 and 9 inhibitors: Anticancer activity data with prominent cell cycle arrest and DNA fragmentation analysis effects. *Bioorganic Chem.* **2020**, *101*, 103992. [[CrossRef](#)] [[PubMed](#)]
44. Halawa, A.H.; El-Gilil, S.M.A.; Bedair, A.H.; Eliwa, E.M.; Frese, M.; Sewald, N.; Shaaban, M.; El-Agrody, A.M. Synthesis of diverse amide linked bis-indoles and indole derivatives bearing coumarin-based moiety: Cytotoxicity and molecular docking investigations. *Med. Chem. Res.* **2018**, *27*, 796–806. [[CrossRef](#)]
45. Eliwa, E.M.; Abdel-Razek, A.S.; Frese, M.; Wibberg, D.; Halawa, A.H.; El-Agrody, A.M.; Bedair, A.H.; Kalinowski, J.; Sewald, N.; Shaaban, M. New bioactive compounds from the marine-derived actinomycete *Nocardioopsis lucentensis* sp. ASMR2. *Z. Nat. B* **2017**, *72*, 351–360. [[CrossRef](#)]
46. El-Agrody, A.M.; Al-Omar, M.A.; Amr, A.-G.E.; Chia, T.S.; Fun, H.-K. Ethyl 2-amino-4-(4-fluorophenyl)-6-methoxy-4H-benzo[h]chromene-3-carboxylate. *Acta Crystallogr. Sect. E Struct. Rep. Online* **2012**, *68*, o1803–o1804. [[CrossRef](#)] [[PubMed](#)]
47. El-Agrody, A.M.; Afifi, T.H. The Reactivity of 8-Hydroxyquinoline and Its Derivatives Toward. alpha.-Cyanocinnamionitriles and Ethyl. alpha.-Cyanocinnamates: Synthesis, Reactions, and Applications of 4H-Pyrano [3, 2-h] quinoline Derivatives. *Heterocycles* **2014**, *89*, 1557–1584. [[CrossRef](#)]
48. El Gaafary, M.; Lehner, J.; Fouda, A.M.; Hamed, A.; Ulrich, J.; Simmet, T.; Syrovets, T.; El-Agrody, A.M. Synthesis and evaluation of antitumor activity of 9-methoxy-1H-benzo[f]chromene derivatives. *Bioorganic Chem.* **2021**, *116*, 105402. [[CrossRef](#)]
49. El-Mawgoud, H.K.A.; Fouda, A.M.; El-Nassag, M.A.A.; Elhenawy, A.A.; Alshahrani, M.Y.; El-Agrody, A.M. Discovery of novel rigid analogs of 2-naphthol with potent anticancer activity through multi-target topoisomerase I & II and tyrosine kinase receptor EGFR & VEGFR-2 inhibition mechanism. *Chem. -Biol. Interact.* **2022**, *355*, 109838. [[CrossRef](#)]
50. Elgaafary, M.; Fouda, A.M.; Mohamed, H.M.; Hamed, A.; El-Mawgoud, H.K.; Jin, L.; Ulrich, J.; Simmet, T.; Syrovets, T.; El-Agrody, A.M. Synthesis of β -enaminonitriles linked 8-methoxy-1H-benzo[f]chromene moieties and analysis of their antitumor mechanisms. *Front. Chem.* **2021**, *9*, 759149. [[CrossRef](#)]
51. Mosmann, T. Rapid colorimetric assay for cellular growth and survival: Application to proliferation and cytotoxicity assays. *J. Immunol. Methods* **1983**, *65*, 55–63. [[CrossRef](#)]
52. Ahmed, H.E.; El-Nassag, M.A.; Hassan, A.; Mohamed, H.; Halawa, A.H.; Okasha, R.M.; Ihmaid, S.; El-Gilil, S.M.A.; Khattab, E.S.; Fouda, A.M.; et al. Developing lipophilic aromatic halogenated fused systems with specific ring orientations, leading to potent anticancer analogs and targeting the c-Src Kinase enzyme. *J. Mol. Struct.* **2019**, *1186*, 212–223. [[CrossRef](#)]
53. Antonello, A.; Tarozzi, A.; Morroni, F.; Cavalli, A.; Rosini, M.; Hrelia, P.; Bolognesi, M.L.; Melchiorre, C. Multitarget-Directed Drug Design Strategy: A Novel Molecule Designed To Block Epidermal Growth Factor Receptor (EGFR) and To Exert Proapoptotic Effects. *J. Med. Chem.* **2006**, *49*, 6642–6645. [[CrossRef](#)]
54. Tabernero, J. The Role of VEGF and EGFR Inhibition: Implications for Combining Anti-VEGF and Anti-EGFR Agents. *Mol. Cancer Res.* **2007**, *5*, 203–220. [[CrossRef](#)] [[PubMed](#)]

55. Mghwary, A.E.-S.; Gedawy, E.M.; Kamal, A.M.; Abuel-Maaty, S.M. Novel thienopyrimidine derivatives as dual EGFR and VEGFR-2 inhibitors: Design, synthesis, anticancer activity and effect on cell cycle profile. *J. Enzym. Inhib. Med. Chem.* **2019**, *34*, 838–852. [[CrossRef](#)] [[PubMed](#)]
56. Henkelman, G.; Arnaldsson, A.; Jónsson, H. A fast and robust algorithm for Bader decomposition of charge density. *Comput. Mater. Sci.* **2003**, *36*, 354–360. [[CrossRef](#)]
57. Koch, U.; Popelier, P.L. Characterization of CHO hydrogen bonds on the basis of the charge density. *J. Phys. Chem.* **1995**, *99*, 9747–9754. [[CrossRef](#)]
58. Bochevarov, A.D.; Harder, E.; Hughes, T.F.; Greenwood, J.R.; Braden, D.A.; Philipp, D.M.; Rinaldo, D.; Halls, M.D.; Zhang, J.; Friesner, R.A. Jaguar: A high-performance quantum chemistry software program with strengths in life and materials sciences. *Int. J. Quantum Chem.* **2013**, *113*, 2110–2142. [[CrossRef](#)]
59. Zhou, X.-Y.; Rong, C.; Lu, T.; Zhou, P.; Liu, S. Information Functional Theory: Electronic Properties as Functionals of Information for Atoms and Molecules. *J. Phys. Chem. A* **2016**, *120*, 3634–3642. [[CrossRef](#)]
60. Sameeh, M.Y.; Khowdiary, M.M.; Nassar, H.S.; Abdelall, M.M.; Alderhami, S.A.; Elhenawy, A.A. Discovery Potent of Thiazolidinedione Derivatives as Antioxidant, α -Amylase Inhibitor, and Antidiabetic Agent. *Biomedicines* **2021**, *10*, 24. [[CrossRef](#)]
61. Bultinck, P.; Winter, H.D.; Langenaeker, W.; Tollenare, J.P. *Computational Medicinal Chemistry for Drug Discovery*; CRC Press: Boca Raton, FL, USA, 2003.
62. Fouda, A.M.; El-Nassag, M.A.; Elhenawy, A.A.; Shati, A.A.; Alfaifi, M.Y.; Elbehairi, S.E.I.; Alam, M.M.; El-Agrody, A.M. Synthesis of 1,4-dihydropyrano[2,3-c]pyrazole derivatives and exploring molecular and cytotoxic properties based on DFT and molecular docking studies. *J. Mol. Struct.* **2022**, *1249*, 131555. [[CrossRef](#)]
63. Alzahrani, H.A.; Alam, M.M.; Elhenawy, A.A.; Malebari, A.M.; Nazreen, S. Synthesis, antiproliferative, docking and DFT studies of benzimidazole derivatives as EGFR inhibitors. *J. Mol. Struct.* **2022**, *1253*, 132265. [[CrossRef](#)]
64. Ali, I.O.; Nassar, H.S.; El-Nasser, K.S.; Bougarech, A.; Abid, M.; Elhenawy, A.A. Synthesis and characterization of MnII and CoII complexes with poly (vinyl alcohol-nicotinic acid) for photocatalytic degradation of Indigo carmine dye. *Inorg. Chem. Commun.* **2021**, *124*, 108360. [[CrossRef](#)]
65. Politzer, P.; Murray, J.S.; Bulat, F.A. Average local ionization energy: A review. *J. Mol. Model.* **2010**, *16*, 1731–1742. [[CrossRef](#)]
66. Omar, A.M.M.; AboulWafa, O.M.; Amr, M.E.; El-Shoukrofy, M.S. Antiproliferative activity, enzymatic inhibition and apoptosis-promoting effects of benzoxazole-based hybrids on human breast cancer cells. *Bioorganic Chem.* **2021**, *109*, 104752. [[CrossRef](#)]
67. Saha, B.; Thapa, R.; Chattopadhyay, K. Bandgap widening in highly conducting CdO thin film by Ti incorporation through radio frequency magnetron sputtering technique. *Solid State Commun.* **2008**, *145*, 33–37. [[CrossRef](#)]
68. Siemens Analytical X-Ray Instruments, Inc. *Anal. Chem.* **1990**, *62*, 413A. [[CrossRef](#)]
69. Mackenzie, C.F.; Spackman, P.R.; Jayatilaka, D.; Spackman, M.A. CrystalExplorer model energies and energy frameworks: Extension to metal coordination compounds, organic salts, solvates and open-shell systems. *IUCrJ* **2017**, *4*, 575–587. [[CrossRef](#)]
70. Frisch, G.W.T.M.J.; Schlegel, H.B.; Scuseria, G.E.; Robb, M.A.; Cheeseman, J.R.; Scalmani, G.; Barone, V.; Mennucci, B.; Petersson, G.A.; Nakatsuji, H.; et al. *Toyota, Gaussian 09, Revision*; Gaussian, Inc.: Wallingford, CT, USA, 2013.
71. Schrödinger, M. *Schrödinger, Schrödinger Release 2018-1*; Schrödinger: New York, NY, USA, 2018.